








## Elastic scattering investigation of radioactive $^{13}\text{B}$ and $^{13}\text{O}$ projectiles on a $^{208}\text{Pb}$ target at intermediate energies

K. Wang <sup>1</sup>, Y. Y. Yang,<sup>1,2,\*</sup> V. Guimarães <sup>3,†</sup>, D. Y. Pang,<sup>4</sup> F. F. Duan,<sup>1</sup> Z. Y. Sun <sup>1,2</sup>, Jin Lei,<sup>5,6</sup> G. Yang,<sup>1,2</sup> S. W. Xu,<sup>1</sup> J. B. Ma,<sup>1</sup> Q. Liu,<sup>7</sup> Z. Bai,<sup>1</sup> H. J. Ong <sup>1,2</sup>, B. F. Lv,<sup>1</sup> S. Guo <sup>1,2</sup>, X. H. Wang <sup>1</sup>, R. H. Li <sup>1</sup>, M. Kumar Raju,<sup>1,‡</sup> Z. G. Hu,<sup>1,2</sup> and H. S. Xu<sup>1,2</sup>

(RIBLL Collaboration)

<sup>1</sup>CAS Key Laboratory of High Precision Nuclear Spectroscopy, Institute of Modern Physics, Chinese Academy of Sciences, Lanzhou 730000, China

<sup>2</sup>School of Nuclear Science and Technology, University of Chinese Academy of Sciences, Beijing 100080, China

<sup>3</sup>Instituto de Física, Universidade de São Paulo, Rua do Matão, 1371, São Paulo 05508-090, SP, Brazil

<sup>4</sup>School of Physics and Beijing Key Laboratory of Advanced Nuclear Materials and Physics, Beihang University, Beijing, 100191, China

<sup>5</sup>School of Physics Science and Engineering, Tongji University, Shanghai 200092, China

<sup>6</sup>Institute for Advanced Study of Tongji University, Shanghai 200092, China

<sup>7</sup>School of Physics and Materials Science, Anhui University, Hefei 230601, China



(Received 17 February 2022; revised 26 April 2022; accepted 16 May 2022; published 31 May 2022)

Elastic scattering measurements were performed for the proton drip-line nucleus  $^{13}\text{O}$  (with  $S_p = 1.512$  MeV) and its partner mirror nucleus  $^{13}\text{B}$  (with  $S_n = 4.878$  MeV) projectiles on a  $^{208}\text{Pb}$  target at intermediate energies, namely  $E_{\text{lab}} = 413$  and  $254$  MeV, respectively. These secondary radioactive ion beams were produced at the Radioactive Ion Beam Line in Lanzhou (RIBLL), Heavy-Ion Research Facility in Lanzhou (HIRFL). The elastic scattering angular distributions for these projectiles show a typical Fresnel diffraction peak at forward angles. Optical model analyses of the angular distributions, using double-folding and global potentials, were performed and different densities for these projectiles were probed.

DOI: [10.1103/PhysRevC.105.054616](https://doi.org/10.1103/PhysRevC.105.054616)

### I. INTRODUCTION

Elastic scattering is the simplest two-body interaction process in which the states of projectile and target do not change during the collision. However, the study of elastic scattering can provide information on the dynamic effects, as well as on the structure of the colliding nuclei, e.g., weakly bound and halo structure of the projectile. In the past, elastic scattering studies have been widely performed in the literature to understand the heavy-ion interaction [1–3]. With the advent of facilities, which allow the acceleration of radioactive beams, these works have been extended to the investigation of the structure of weakly bound neutron-rich and proton-rich nuclei [4,5]. New nuclear structures have been discovered in these nuclei, such as the existence of a halo structure, where one or two valence nucleons are loosely bound to a core nucleus, forming an extended matter distribution [6].

The theoretical study of the elastic scattering is a well-known inverse problem in quantum scattering theory. The Woods-Saxon shape potential has been used for the two-body interaction, where the six free parameters can be obtained

by fitting experimental angular distributions [1]. However, in this case, to better determine the potentials involved in the collision, it is important to measure cross sections with high precision and over a wide angular range. Additionally, a high-quality and wide angular distribution allows a better investigation of the influence of particular nuclear structure properties of the collision partners. Actually, the investigation of the interplay between nuclear structure and reaction mechanism is active in nuclear physics due to the strong synergy between the configuration nature of the exotic and weakly bound (stable and radioactive) nuclei and the dynamics of the processes involved in the nuclear reaction [7,8].

The elastic scattering angular distributions may be affected by the nuclear structure, the size and density of the interacting nuclei, which are quite different for tightly bound and weakly bound ones. For instance, the low binding energy and peculiar structure of some exotic nuclei can enhance the breakup and/or transfer cross sections, introducing characteristic dynamic polarization (attractive or repulsive) in the optical potential, which is not present in the elastic scattering induced by tightly bound nuclei. To investigate the absorption effect of the nuclear potential, due to deformation, cluster configuration and/or low binding energy of the projectile, several elastic scattering measurements for weakly bound nuclei have been performed on the heavy  $^{208}\text{Pb}$  target, in which long-range nuclear interactions and Coulomb dipole polarizability effects are expected to be stronger [4,5]. For instance, the influence of

\*Corresponding author: yangyanyun@impcas.ac.cn

†Corresponding author: valdirg@if.usp.br

‡Present address: Department of Physics, GITAM Institute of Science, GITAM University, Visakhapatnam-530045, India

these effects in the elastic scattering cross section was investigated by a phenomenological analysis reported in Ref. [9], where a relationship between the critical interaction distance and binding energy for a given cluster configuration is studied.

Several elastic scattering experiments were performed at energies around the Coulomb barriers. However, by extending the energy range from close to the barrier to well above the barrier energies we can increase the scope of elastic scattering investigation. At higher energies one would expect a smaller multistep effects, which may appear due to the inelastic excitation, as the collision time is also smaller. Actually, elastic scattering experiments for the proton drip-line nucleus  ${}^8\text{B}$  have been recently performed at energies close to [10,11] and above [12–14] the Coulomb barrier, with interesting results, mainly due to the very weakly bound valence proton ( $S_p = 0.1375$  MeV) in  ${}^8\text{B}$ . For the measurements at higher energies, the influence of the breakup channel was found to be only modest in the description of the elastic scattering angular distributions of  ${}^8\text{B}$  on  ${}^{208}\text{Pb}$ . On the other hand, the recent performed experiment for the neutron-rich  ${}^{11}\text{Be}$  projectile [15], at energies around three times the Coulomb barrier, showed a surprisingly strong damping of the Fresnel peak in the measured elastic scattering angular distribution, as first observed in the previous studies at near-barrier energies [16–18]. This result is a clear indication that the extra long-range absorptive contribution, due to the weak nature of the valence neutron in  ${}^{11}\text{Be}$ , manifest at both close to and above the barrier energies regime. This effect was not observed in the elastic scattering of tightly bound  ${}^{10}\text{Be}$  projectile on  ${}^{208}\text{Pb}$  target at either close to [19] or above the barrier energies [20].

The proton drip-line nucleus  ${}^{13}\text{O}$  and its partner mirror  ${}^{13}\text{B}$  have attracted some interest over the years. These two nuclei have the same isospin  $T = 3/2$ , with binding energies:  ${}^{13}\text{O} = {}^{12}\text{N} + p$  with  $S_p = 1.512$  MeV and  ${}^{13}\text{B} = {}^{12}\text{B} + n$  with  $S_n = 4.878$  MeV, respectively [21,22]. In the measurements of the interaction cross sections for  ${}^{13}\text{O}$  on Be, C, and Al targets at higher energies, a normal root-mean-square (RMS) proton radius,  $R_{\text{rms}}^m = 2.53 \pm 0.05$  fm was observed for  ${}^{13}\text{O}$  [23], while  $R_{\text{rms}}^m = 2.46 \pm 0.12$  fm was observed for  ${}^{13}\text{B}$  [24]. Conversely, the investigation of quadrupole moment of  ${}^{13}\text{O}$  suggests the existence of a thin proton halo in this nucleus [25]. More recently, the level scheme of  ${}^{13}\text{O}$  was compared to the state-of-the-art *ab initio* no-core shell model calculations [26], which indicates a strong proton  $1s_{1/2}$  structure for the lowest-energy excited states. But to our knowledge, there have been no reports of elastic scattering study of  ${}^{13}\text{O}$  on heavy target, most likely due to the limited beam intensity this particular nucleus can be produced. In the present work we report on the investigation of the elastic scattering of the proton-rich  ${}^{13}\text{O}$  and neutron-rich  ${}^{13}\text{B}$  projectiles on  ${}^{208}\text{Pb}$  target, at energies well above the Coulomb barrier. The aim of this study is to investigate the elastic process induced by these radioactive ion beams on a heavy target, which has been measured for the first time. The new data for the elastic scattering angular distributions were compared to optical model calculations using different potentials. A detailed description of the experimental setup and procedure is given in Sec. II. The measured elastic scattering angular distributions

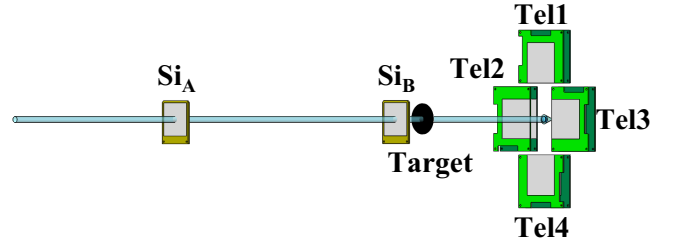


FIG. 1. Sketch of the detector setup. The two DSSDs ( $\text{Si}_A$  and  $\text{Si}_B$ ) were placed upstream from the target to measure the beam position. The reaction products were detected by the four telescopes mounted around the beam axis.

for  ${}^{13}\text{B}$  and  ${}^{13}\text{O}$  and optical model analyses are presented in Sec. III. In Sec. IV, the summary and some conclusions are presented.

## II. EXPERIMENTAL SETUP AND MEASUREMENTS

Angular distributions for the elastic scattering of the  ${}^{13}\text{B}$  and  ${}^{13}\text{O}$  on a  ${}^{208}\text{Pb}$  target at  $E_{\text{lab}} = 254$  and  $413$  MeV, respectively, corresponding to about five times the Coulomb barrier [ $V_B({}^{13}\text{B}) = 48.8$  MeV and  $V_B({}^{13}\text{O}) = 78.0$  MeV] for each system, were measured for the first time. The experiment was performed at the National Laboratory of Heavy Ion Research of the Institute of Modern Physics, Chinese Academy of Sciences (IMPCAS). The secondary  ${}^{13}\text{B}$  and  ${}^{13}\text{O}$  radioactive beams were produced by fragmentation of a primary  $59.54$  MeV/u  ${}^{16}\text{O}^{8+}$  beam, delivered by the Heavy-Ion Research Facility in Lanzhou (HIRFL) [27,28], on a production  ${}^9\text{Be}$  target. The thicknesses of the production target were  $4.5$  mm and  $2.0$  mm for  ${}^{13}\text{B}$  and  ${}^{13}\text{O}$  beams, respectively. After the production, the  ${}^{13}\text{B}$  and  ${}^{13}\text{O}$  radioactive beams were purified by magnetic rigidity ( $B\rho$ ) with the Radioactive Ion Beam Line in Lanzhou (RIBLL) [29,30] and focused on a  $12.24\text{-mg/cm}^2$ -thick self-supporting  ${}^{208}\text{Pb}$  target. The average intensities of  ${}^{13}\text{B}$  and  ${}^{13}\text{O}$  beams were approximately  $1500$  and  $200$  pps, with purities of  $53\%$  and  $2\%$ , respectively. The beam energies at the center of the target were about  $E_{\text{lab}} = 254$  MeV and  $413$  MeV for  ${}^{13}\text{B}$  and  ${}^{13}\text{O}$ , respectively. These secondary beams were identified and discriminated by using a combination of time-of-flight (ToF) and magnetic rigidity ( $B\rho$ ) signals. The ToF detectors consisted of two plastic scintillators ( $\text{C}_9\text{H}_{10}$ ),  $50$   $\mu\text{m}$ -thick, installed at the second (F2) and fourth (F4) focal plane of RIBLL, giving a total of  $1680$  cm flight length.

The schematic view of the detector setup used in the present experiment is shown in Fig. 1. Two double-sided silicon strip detectors (DSSDs),  $87$   $\mu\text{m}$  ( $\text{Si}_A$ ) and  $65$   $\mu\text{m}$  ( $\text{Si}_B$ ) thick, both segmented into  $16$  horizontal and vertical strips ( $3\text{-mm}$  width on each side), were used to provide precise position and direction of the incident beam particles, on an event-by-event basis. These two DSSDs were placed  $669$  mm and  $69$  mm upstream the  ${}^{208}\text{Pb}$  target, respectively, as indicated in Fig. 1. The elastically scattered and reaction products were detected by an array of four silicon telescopes, namely,

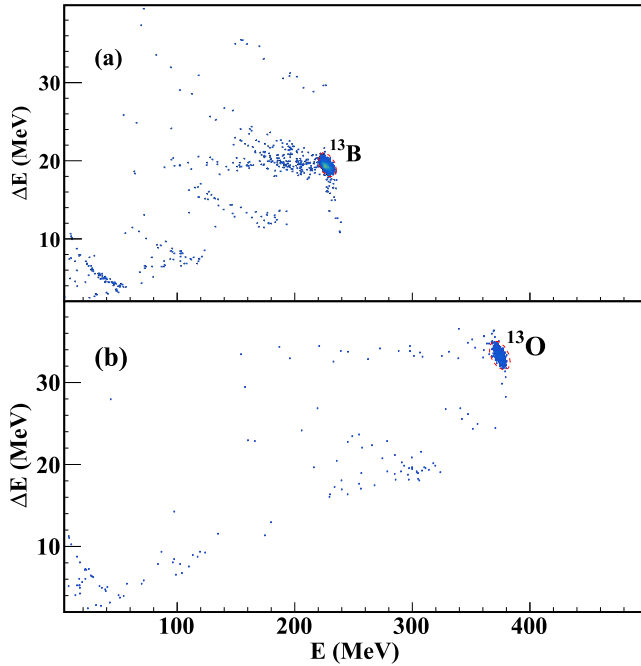


FIG. 2. (a) The calibrated two-dimensional  $\Delta E - E$  particle identification spectrum with a time window on the  $^{13}\text{B}$  projectile obtained by Tel2; (b) the same spectrum but with a time window on the  $^{13}\text{O}$  projectile.

Tel1, Tel2, Tel3, and Tel4, mounted 267 mm away from the lead target. These telescopes covered an angular range from  $3^\circ - 27^\circ$  in the laboratory frame, with a resolution of about  $0.4^\circ$ . Each telescope consisted of a DSSD ( $32 \times 32$  pixels,  $64 \times 64 \text{ mm}^2$ ) with  $\Delta E$  detector  $\approx 150 \mu\text{m}$  thick backed by a silicon  $E$  detector  $\approx 1,500 \mu\text{m}$  thick, which measured the residual energy of the particles. To ensure a satisfactory performance, the temperature of this detector array was kept at  $-20^\circ\text{C}$  during the whole experiment, using an alcohol circulating system.

A good separation of the  $^{13}\text{B}$ ,  $^{13}\text{O}$  secondary beams from the possible beam contaminants is crucial in this experiment. This was achieved owing to the excellent resolution of ToF signals, which is better than 2 ns (full width at half maximum). Typical two-dimensional  $\Delta E - E$  particle identification spectra with ToF restrictions on the  $^{13}\text{B}$  and  $^{13}\text{O}$  beams are shown in Fig. 2(a) and Fig. 2(b), respectively. As can be seen in the figures, the elastically scattered  $^{13}\text{B}$  and  $^{13}\text{O}$  particles can be uniquely identified and are well separated from any beam contaminants.

The angles of the elastic scattering particles and reactions events were determined by considering the incident track direction of the beam particles extrapolated to the target position. The directions of the particles were obtained by the signals from the  $\text{Si}_A$  and  $\text{Si}_B$  detectors in combination with the hit positions in the telescopes. To evaluate the absolute differential cross section, Monte Carlo simulations, assuming pure Rutherford scattering at all angles, taking into account the actual detector setup geometry and the broad and nonuniform beam profiles on the target, were performed. More details on

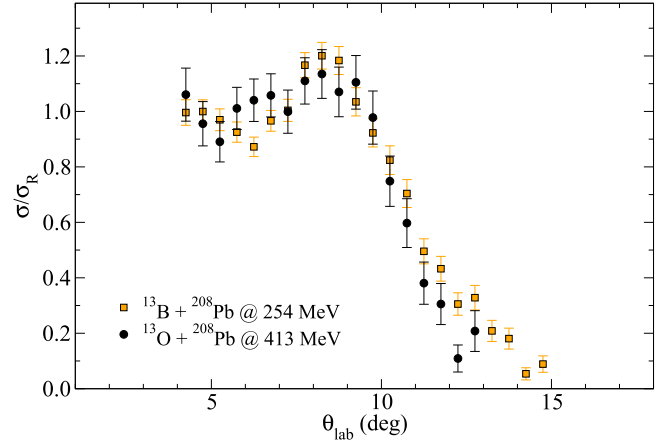


FIG. 3. Elastic scattering angular distribution for  $^{13}\text{B} + ^{208}\text{Pb}$  at  $E_{\text{lab}} = 254 \text{ MeV}$  and for  $^{13}\text{O} + ^{208}\text{Pb}$  at  $E_{\text{lab}} = 413 \text{ MeV}$ . Error bars are due to the statistical uncertainty only.

the procedure to obtain the cross sections and to minimize the systematic errors, are given in Refs. [12,14,31].

The cross sections for the angular distribution for both  $^{13}\text{B}$  and  $^{13}\text{O}$  were measured at  $\theta_{\text{lab}} = 4^\circ - 15^\circ$ . A global normalization factor for the measured cross sections was determined considering the elastic scattering cross sections of  $^{11}\text{C} + ^{208}\text{Pb}$  at  $E_{\text{lab}} = 275 \text{ MeV}$ , which were assumed pure Rutherford scattering at forward angles [12]. This global normalization was applied to the angular distributions for  $^{13}\text{B} + ^{208}\text{Pb}$  at  $E_{\text{lab}} = 254 \text{ MeV}$  and  $^{13}\text{O} + ^{208}\text{Pb}$  at  $E_{\text{lab}} = 413 \text{ MeV}$ . These angular distributions in terms of differential cross section ratio to the Rutherford cross section ( $\sigma/\sigma_{\text{Ruth}}$ ) are shown in Fig. 3. The uncertainties in the cross sections are purely statistical. The error bars are smaller for  $^{13}\text{B}$  projectile as compared to  $^{13}\text{O}$  since the beam intensity was much higher for  $^{13}\text{B}$  radioactive beam. We should mention that, in principle, since we could not discriminate the elastic and inelastic scattering from the excited states of the lead target nucleus, the data are of quasielastic nature. However, the contributions from the excited states of the lead target have been found to be negligible in several experiments with the similar mass projectile, angular range, and energy as considered in this experiment [12,13]. The  $^{13}\text{O}$  projectile has no bound states and although  $^{13}\text{B}$  projectile has some excited states in between 3.5–4.5 MeV, their influence on the elastic scattering should be quite small due to the high excitation energies and small values for the  $B(E2)$  of these states [32,33]. For these reasons we are considering and mentioning the data as elastic scattering data along this paper. The angular range, covered by these angular distributions, includes the Fresnel peak region for both systems, which is important to investigate the characteristics of the interaction potential. Since both data are about 5.0 times the coulomb barrier we can compare the two angular distributions, as shown in Fig. 3. Despite the error bars of the cross sections, it is clear that the Coulomb-nuclear peak of the elastic scattering angular distribution for the  $^{13}\text{O}$  projectile is slightly suppressed as compared to that for  $^{13}\text{B}$ . As discussed in Ref. [2], this kind of suppression might be due to the couplings to inelastic or to the continuum. In our case,  $^{13}\text{O}$

nucleus has a lower binding energy (1.512 MeV), compared to  $^{13}\text{B}$ , and thus, the coupling to the continuum might be more important. Usually, the couplings effect can be observed as deviation of elastic flux from the Coulomb-nuclear peak to the backward angles. The coupling to the continuum for the weakly bound  $^{13}\text{O}$  projectile is discussed in the next section. Also, by comparing the angular distributions of  $^{13}\text{O}$  and  $^{13}\text{B}$ , we can observe that the cross sections at backward angles are larger for  $^{13}\text{B}$  due to a little stronger absorption for the  $^{13}\text{O}$  projectile, probably by the breakup (coupling to continuum) channel.

### III. DATA ANALYSIS AND RESULTS

The angular distributions for the elastic scattering of  $^{13}\text{B}$  and  $^{13}\text{O}$  were analyzed in terms of the optical model (OM) with different approaches. In this phenomenological analysis, the interaction between the colliding nuclei is represented by a complex potential. Although the intrinsic structure properties of the collision partners are not explicitly taken into account in this approach, the description of the cross sections for elastic scattering is very sensitive to the interaction potential between the projectile and the target nuclei and to the properties of their structures, such as the radius and diffuseness of their nucleon density distributions.

For the nuclear potential we first considered the double-folding São Paulo potential (SPP) in its new version São Paulo potential-2 (SPP2) [34], which is an improvement of the previous version [35]. As the first version, the SPP2 is a potential of double convolution on the nuclear densities of the projectile and target and it can then be used in association with the optical model, with  $N_R$  and  $N_I$  as the normalization factor for the real and imaginary part, respectively. It is important to mention that the convolution is over the nucleon distribution and not on the nuclear matter distribution. The nucleon distribution in this model is given by the sum of the proton and neutron densities, which, by its turn, are determined by considering the intrinsic matter density of a nucleon with the charge density of a proton. Thus, the nuclear potential is determined by the nuclear matter densities of the colliding nuclei and the effective nuclear interaction between two elements of matter. See Ref. [34] for further details on the model. By adopting standard values for the normalization ( $N_R = 1.00$  and  $N_I = 0.78$ ), obtained from a large systematic analysis, the calculation with SPP can be considered as with no free parameters. The new version SPP2 considers the charge densities in the determination of the nucleon distribution, which can be obtained by two ways: (i) from an external file with extracted values from electron scattering experiments, which can be relate as the experimental determination of matter densities and (ii) from calculated values (inside the code) using an axially symmetric self-consistent Dirac-Hartree-Bogoliubov (DHB) mean-field approximation to the nuclear ground state [36]. In the present work, since there is no electron scattering experiment on the radioactive  $^{13}\text{B}$  and  $^{13}\text{O}$  nuclei, we considered the calculated values of the option (ii) for the matter densities.

The results of OM calculation with the SPP2 is shown in Figs. 4 and 5. The calculations can describe well the angular

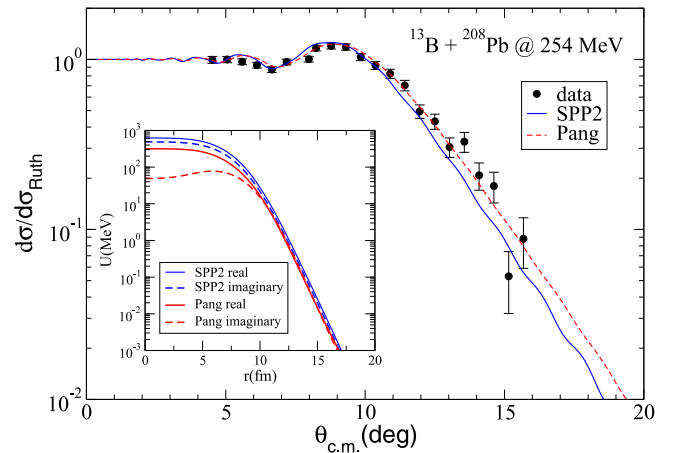


FIG. 4. Angular distribution for the  $^{13}\text{B} + ^{208}\text{Pb}$  system at 254 MeV. The curves are the results for the optical model analysis with the potentials as indicated. See text for explanation.

distribution for the most forward angles up to the Fresnel peak region. However, the calculations underestimate a little of the data for the most backward angles for  $^{13}\text{B}$  and overestimating those for  $^{13}\text{O}$ . It is important to mention that we did not adjust any parameter in the calculation. The new SPP2 as the previous version of the SPP should be considered just as comparative standard calculation. Deviation of such calculations may indicate that some other important effect may be playing a role in the collision, increasing or diminishing the absorption of the elastic flux. A better agreement between the SPP2 calculation and the data may be achieved by changing the normalization of the real and/or imaginary potentials or by considering a Woods-Saxon shape (with three free parameters) for the imaginary potential. However, in this case, the physics of the effect would be hidden in the normalization parameters.

Another kind of potential, which can be applied in the analysis of elastic scattering data is global or systematic potentials. In the optical model analysis for elastic scattering at not so

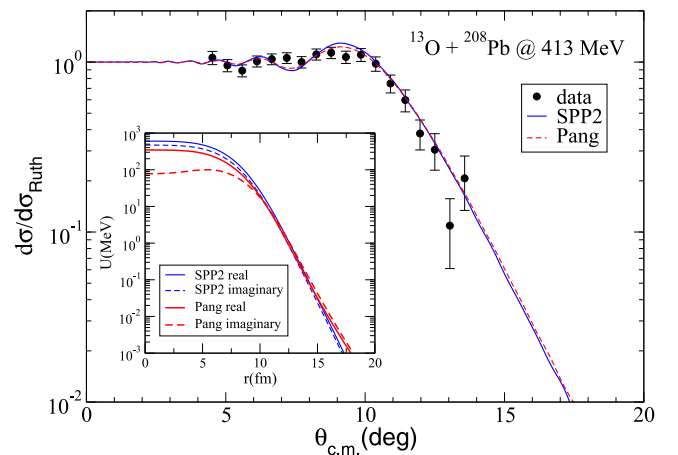


FIG. 5. Angular distribution for the  $^{13}\text{O} + ^{208}\text{Pb}$  system at 413 MeV. The curves are the results for the optical model analysis with the potentials as indicated. See text for explanation.

high energy, the angular distribution is more sensitive to the superficial part of the potentials, and, thus, sets of parameters, producing a similar potential at the surface region, would give equivalent description of the data [37]. However, by considering a wide range of masses for the projectile and/or target, global or systematic potentials may reduce these ambiguities in the optical model potential. Global potentials from systematic analysis have been obtained from the investigation of nuclear reactions induced by radioactive nuclei [38–40] and applied in association with optical model. Here we considered a global nucleus-nucleus potential, obtained from a systematic optical potential analysis by Xu and Pang [41]. This global potential could reasonably account for elastic scattering and total reaction cross sections for projectile with mass numbers up to  $A < 40$ , including both stable and unstable nuclei and at the energies above the Coulomb barrier. This nucleus-nucleus potential is based on a single-folding model potential with a semimicroscopic Jeukenne-Lejeune-Mahaux-Bruyères (JLMB) potential type [42]. The density distributions of the projectile and target nuclei are necessary in the process of calculation using a single-folding potential. The density distribution of the projectile can be deduced from the observed interaction cross section and total reaction cross section by Glauber-model analysis [43], and also by Hartree-Fock calculation [44]. In the present work, we used the nucleon density distributions from Hartree-Fock calculations with the SkX interaction [44] in the single-folding model calculations, with the RMS matter radii of 2.534 and 2.578 fm for  $^{13}\text{B}$  and  $^{13}\text{O}$ , respectively.

The results of the calculations with the Pang global potential for the  $^{13}\text{B} + ^{208}\text{Pb}$  and  $^{13}\text{O} + ^{208}\text{Pb}$  systems are also shown in Figs. 4 and 5 by red dashed lines. Overall, the calculations agree quite well with the experimental data. Both potentials are compared in the inset of Figs. 4 and 5 where we plot the depth of the potential as a function of the distance. The potential for the elastic scattering process is more sensitive at the distance of strong absorption. Considering the quarter-point receipt, this distance of strong absorption can be obtained converting the angle, where the ratio of the cross section to the Rutherford cross section is 0.25, to distance of the closest approach [45]. The strong absorption distance is found to be 11.7 fm for  $^{13}\text{B}$  and 11.9 fm for  $^{13}\text{O}$  projectile. Since the strong absorption distance is a little further for  $^{13}\text{O}$ , we expect just a little more absorption for  $^{13}\text{O}$  at backward angles, as, indeed, it is observed in Fig. 3. These distances are also just a little larger than  $R = r_0(A_p^{1/3} + A_t^{1/3}) = 10.75$  fm, and, we can say they are still located at the surface region of the potentials. At this region, it is also possible to observe that the depth of the imaginary SPP2 and Pang are about the same for  $^{13}\text{O}$ , giving thus, the same results for the angular distribution, and the imaginary SPP2 is a little deeper for the  $^{13}\text{B}$ , producing a bit more absorption in the calculated angular distribution for the  $^{13}\text{B}$  projectile, compared to the results for the Pang global potential.

Additionally, the calculated elastic scattering angular distribution depends on the given density distribution of the projectile, and, therefore, it can be used to extract their RMS radii by comparing with the experimental data. The systematic optical model results with different density distributions for

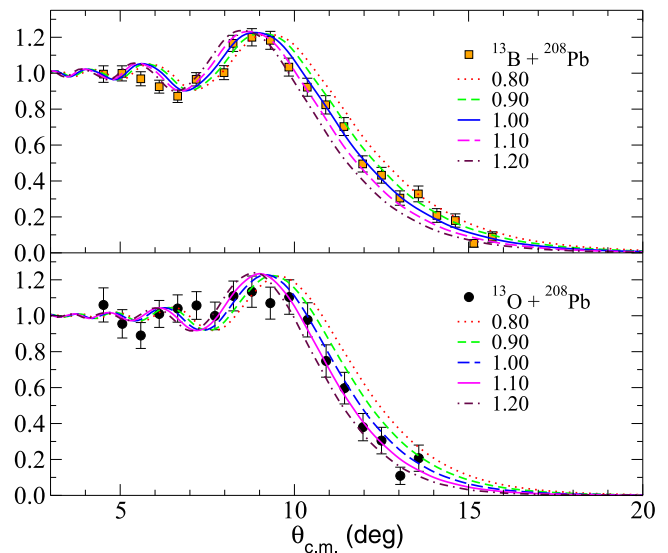


FIG. 6. Angular distributions for the  $^{13}\text{B} + ^{208}\text{Pb}$  system at 254 MeV and for the  $^{13}\text{O} + ^{208}\text{Pb}$  system at 413 MeV. The curves are the results for the global potentials with different density distributions.

$^{13}\text{B}$  and  $^{13}\text{O}$ , and the comparisons with the angular distributions for  $^{13}\text{B} + ^{208}\text{Pb}$  and  $^{13}\text{O} + ^{208}\text{Pb}$  are shown in Fig. 6. These densities are obtained by stretching the original HF densities (as used in Figs. 4 and 5) so that the root-mean-square radii of the resulting nucleon density distributions varied by factors from 0.8–1.2 with respect to their original values. Standard minimum  $\chi^2$  values, defined as  $\frac{1}{N}$ , are used to quantify the agreement between the theoretical angular distributions, calculated with these density distributions, and the experimental data. The results are shown in Fig. 7, where the  $\chi^2$  values are plotted as functions of the stretching factors for  $^{13}\text{B}$  and  $^{13}\text{O}$ , respectively. The optimum proton, neutron, and

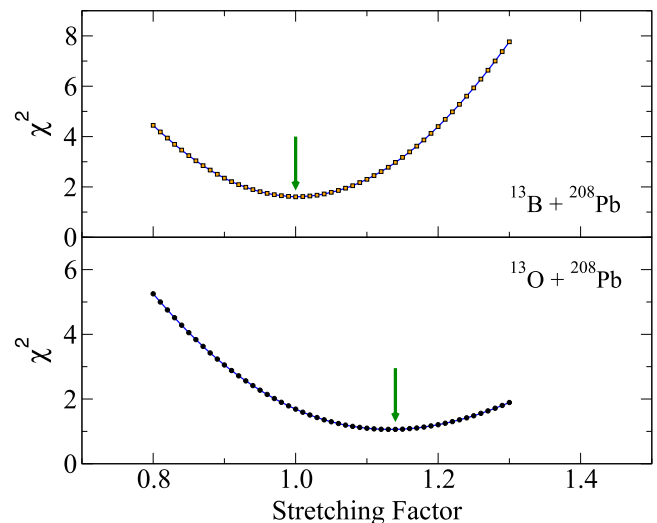


FIG. 7.  $\chi^2$  values obtained for different density distributions in the global potential calculations. The green arrows indicate the minimum  $\chi^2$ . See text for explanation.

TABLE I. The deduced RMS radii of proton, neutron, and matter in this work, in fermis.

	$\langle r_p^2 \rangle^{1/2}$	$\langle r_n^2 \rangle^{1/2}$	$\langle r^2 \rangle^{1/2}$
$^{13}\text{B}$	2.354	2.641	2.534
$^{13}\text{O}$	3.095	2.670	2.939

nuclear matter radii, from these calculations, are summarized in Table I. The extracted matter radius for  $^{13}\text{B}$  is the same as the result from Hartree-Fock calculation. However, the radius of  $^{13}\text{O}$  is 1.14 times larger than the one from Hartree-Fock calculation. This may indicate an exotic structure of the drip-line nucleus  $^{13}\text{O}$ , which is consistent with the possible existence of a thin proton halo in Ref. [25].

The proton energy separation,  $S_p = 1.512$  MeV, for the  $^{13}\text{O}$  projectile can be considered low and breakup channel might be playing a role in the collision induced by this radioactive nucleus. The importance of the breakup coupling effect in the elastic scattering for  $^{13}\text{O}$  can be estimated by performing continuum discretized coupled channels (CDCC) calculations, which was performed with the code FRESKO [46]. In the calculation,  $^{13}\text{O}$  was modeled as consisting of an  $^{12}\text{N}$  core and a valence proton. We considered the possibility of this valence proton to be either in the  $1p$  or  $2s$  orbital. For simplicity, the spins of both the proton and the  $^{12}\text{N}$  nucleus were omitted. The  $p$ - $^{12}\text{N}$  binding potential was of Woods-Saxon form with parameters  $r_0 = 1.25$  fm and  $a_0 = 0.65$  fm. The potential depth was adjusted to give the proton binding energy (1.512 MeV) for the ground state of  $^{13}\text{O}$ . The discretized bin states were built considering that they are equally spaced in momentum space, with maximum energy of  $\epsilon_{\text{bin}} = 22.65$  MeV. The potential multipoles were considered up to  $\lambda \leq 3$ . The complex optical potentials, necessary to describe the  $^{12}\text{N}$ - $^{208}\text{Pb}$  and  $p$ - $^{208}\text{Pb}$  systems, were taken as the systematic single-folding potential [41] and KD02 systematics [47], respectively.

The results of the CDCC calculations are shown in Fig. 8 for both  $1p$  and  $2s$  configurations of the valence proton in  $^{13}\text{O}$ . The calculations describe quite well the experimental angular distributions. We would like to emphasize that these calculations are parameter free. As can be qualitatively observed in the figure, the coupling effect of the CDCC calculations on the reaction mechanism is deviating the elastic flow from forward angles to backward angles. Although small, this effect improves the description of the experimental angular distribution, mainly at the Fresnel peak, as compared to the no-coupling calculation.

$^{13}\text{O}$  nucleus has no bound states but the excited states of the  $^{13}\text{B}$  nucleus have attracted some attention. Investigation on the structure of the isotones with  $N = 8$ , having  $^{13}\text{B}$  nucleus between the  $^{12}\text{Be}$  and  $^{14}\text{C}$ , is related to the fading of the shell closure [33,48,49]. It has been observed that with the increasing of the  $N/Z$  asymmetry, unusual rearrangements of single-particle orbitals can emerge (intruder states), breaking down the usual  $N = 8$  magic number. In this sense, positive parity states in  $^{13}\text{B}$  would correspond to neutron excitation and gap between  $sp$  and  $sd$  shells. The structure of  $^{13}\text{B}$  is

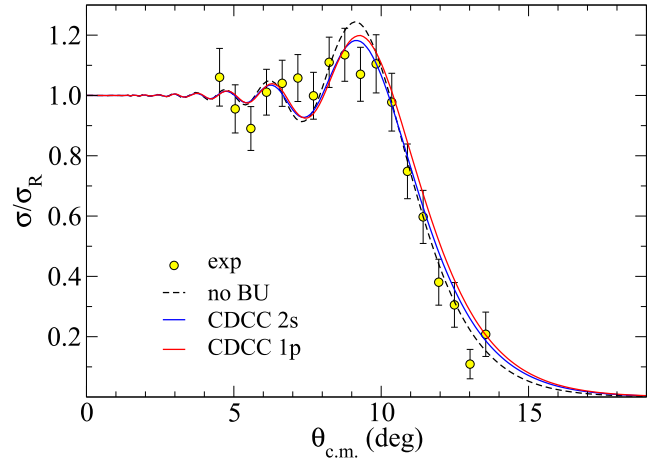


FIG. 8. Angular distribution for the  $^{13}\text{O} + ^{208}\text{Pb}$  system at 413 MeV. The curves are the results of the CDCC calculations with  $1p$  and  $2s$  configurations for the valence proton.

still under investigation. The calculated  $B(E2)$  values, based on some assumptions for spins, are very small [32,33,48,49]. Combining this information with the fact that the excitation energies of these states are in the range of 3.5–4.5 MeV, we would expect a very small contribution of the inelastic scattering. Although we cannot infer too much about the structure of  $^{13}\text{B}$  from our data, the lack of strong coupling to the continuum would be an indication that  $^{13}\text{B}$  is spherical, as it has been shown by antisymmetrized molecular dynamics (AMD) calculations [32], and still holds the  $N = 8$  magicity.

#### IV. SUMMARY AND CONCLUSIONS

Angular distributions for the elastic scattering of the radioactive nuclei  $^{13}\text{B}$  and  $^{13}\text{O}$  on  $^{208}\text{Pb}$  were measured for the first time at energies above the Coulomb barrier at HIRFL-RIBLL. These angular distributions were analyzed with the optical model using different approaches. First, double-folding São Paulo and Pang global potentials were considered in the OM analysis. The latter gave a good description of both angular distributions, in particular in the region of the Fresnel peak, indicating the reliability of this potential. Although all these calculations are parameter free, the agreement could be further improved with a better choice of the density distribution, which allowed the extraction of a RMS radius for  $^{13}\text{B}$  and  $^{13}\text{O}$ .

This work has shown that elastic scattering data, at intermediate energies, can be useful to understand the key role of target-projectile effects on the reaction mechanisms. From a detailed analysis using the global potential, the radii of  $^{13}\text{B}$  and  $^{13}\text{O}$  could be investigated, indicating a possible existence of a thin proton skin for  $^{13}\text{O}$ .

#### ACKNOWLEDGMENTS

We would like to acknowledge the staff of HIRFL for the operation of the cyclotron and their friendly collaboration. This work was financially supported by the National Key

R&D Program of China (Grant No. 2018YFA0404403), the National Natural Science Foundation of China (Grants No. 12122511, No. U2067205, No. 12105330), and the Youth

Innovation Promotion Association CAS (Grant No. 2020411). V.G would like to thank São Paulo Research Foundation (FAPESP) Grant No. 2016/17612-7.

- [1] M. Brandan and G. Satchler, *Phys. Rep.* **285**, 143 (1997).
- [2] N. Keeley, K. W. Kemper, and K. Rusek, *Eur. Phys. J. A* **50**, 145 (2014).
- [3] L. F. Canto, V. Guimarães, J. Lubián, and M. S. Hussein, *Eur. Phys. J. A* **56**, 281 (2020).
- [4] N. Keeley, N. Alamanos, K. Kemper, and K. Rusek, *Prog. Part. Nucl. Phys.* **63**, 396 (2009).
- [5] J. Kolata, V. Guimarães, and E. Aguilera, *Eur. Phys. J. A* **52**, 123 (2016).
- [6] I. Tanihata, H. Savajols, and R. Kanungo, *Prog. Part. Nucl. Phys.* **68**, 215 (2013).
- [7] O. A. Rubtsova, V. I. Kukulin, and A. M. Moro, *Phys. Rev. C* **78**, 034603 (2008).
- [8] P. Capel and F. M. Nunes, *J. Phys.: Conf. Ser.* **312**, 082015 (2011).
- [9] V. Guimarães, J. Lubian, J. J. Kolata, E. F. Aguilera, M. Assunção, and V. Morcelle, *Eur. Phys. J. A* **54**, 223 (2018).
- [10] M. Mazzocco, N. Keeley, A. Boiano, C. Boiano, M. La Commara, C. Manea, C. Parascandolo, D. Pierroutsakou, C. Signorini, E. Strano, D. Torresi, H. Yamaguchi, D. Kahl, L. Acosta, P. Di Meo, J. P. Fernandez-Garcia, T. Glodariu, J. Grebosz, A. Guglielmetti, Y. Hirayama *et al.*, *Phys. Rev. C* **100**, 024602 (2019).
- [11] R. Spartà, A. Di Pietro, P. Figuera, O. Tengblad, A. Moro, I. Martel, J. Fernández-García, J. Lei, L. Acosta, M. Borge, G. Bruni, J. Cederkäll, T. Davinson, J. Ovejas, L. Fraile, D. Galaviz, J. Halkjaer Jensen, B. Jonson, M. La Cognata, A. Perea *et al.*, *Phys. Lett. B* **820**, 136477 (2021).
- [12] Y. Y. Yang, J. S. Wang, Q. Wang, D. Pang, J. B. Ma, M. R. Huang, J. L. Han, P. Ma, S. L. Jin, Z. Bai, Q. Hu, L. Jin, J. B. Chen, N. Keeley, K. Rusek, R. Wada, S. Mukherjee, Z. Y. Sun, R. F. Chen, X. Y. Zhang *et al.*, *Phys. Rev. C* **87**, 044613 (2013).
- [13] Y. Y. Yang, X. Liu, D. Y. Pang, D. Patel, R. F. Chen, J. S. Wang, P. Ma, J. B. Ma, S. L. Jin, Z. Bai, V. Guimarães, Q. Wang, W. H. Ma, F. F. Duan, Z. H. Gao, Y. C. Yu, Z. Y. Sun, Z. G. Hu, S. W. Xu, S. T. Wang *et al.*, *Phys. Rev. C* **98**, 044608 (2018).
- [14] RIBLL Collaboration, K. Wang, Y. Y. Yang, A. M. Moro, V. Guimarães, J. Lei, D. Y. Pang, F. F. Duan, J. L. Lou, J. C. Zamora, J. S. Wang, Z. Y. Sun, H. J. Ong, X. Liu, S. W. Xu, J. B. Ma, P. Ma, Z. Bai, Q. Hu, X. X. Xu, Z. H. Gao, H. S. Xu *et al.*, *Phys. Rev. C* **103**, 024606 (2021).
- [15] F. F. Duan, Y. Y. Yang, K. Wang, A. M. Moro, V. Guimarães, D. Y. Pang, J. S. Wang, Z. Y. Sun, J. Lei, A. Di Pietro, X. Liu, G. Yang, J. B. Ma, P. Ma, S. W. Xu, Z. Bai, X. X. Sun, Q. Hu, J. L. Lou, X. X. Xu *et al.*, *Phys. Lett. B* **811**, 135942 (2020).
- [16] A. Di Pietro, G. Randisi, V. Scuderi, L. Acosta, F. Amorini, M. J. G. Borge, P. Figuera, M. Fisichella, L. M. Fraile, J. Gomez-Camacho, H. Jeppesen, M. Lattuada, I. Martel, M. Milin, A. Musumarra, M. Papa, M. G. Pellegriti, F. Perez-Bernal, R. Raabe, F. Rizzo *et al.*, *Phys. Rev. Lett.* **105**, 022701 (2010).
- [17] A. Di Pietro, V. Scuderi, A. M. Moro, L. Acosta, F. Amorini, M. J. G. Borge, P. Figuera, M. Fisichella, L. M. Fraile, J. Gomez-Camacho, H. Jeppesen, M. Lattuada, I. Martel, M. Milin, A. Musumarra, M. Papa, M. G. Pellegriti, F. Perez-Bernal, R. Raabe, G. Randisi *et al.*, *Phys. Rev. C* **85**, 054607 (2012).
- [18] V. Pseudo, M. J. G. Borge, A. M. Moro, J. A. Lay, E. Nácher, J. Gómez-Camacho, O. Tengblad, L. Acosta, M. Alcorta, M. A. G. Alvarez, C. Andreouiu, P. C. Bender, R. Braid, M. Cubero, A. Di Pietro, J. P. Fernández-García, P. Figuera, M. Fisichella, B. R. Fulton, A. B. Garnsworthy *et al.*, *Phys. Rev. Lett.* **118**, 152502 (2017).
- [19] J. J. Kolata, E. F. Aguilera, F. D. Becchetti, Y. Chen, P. A. DeYoung, H. García-Martínez, J. D. Hinnefeld, J. H. Lupton, E. Martínez-Quiroz, and G. Peaslee, *Phys. Rev. C* **69**, 047601 (2004).
- [20] F.-F. Duan, Y.-Y. Yang, D.-Y. Pang, B.-T. Hu, J.-S. Wang, K. Wang, G. Yang, V. Guimarães, P. Ma, S.-W. Xu, X.-Q. Liu, J.-B. Ma, Z. Bai, Q. Hu, S.-Y. Jin, X.-X. Sun, J.-S. Yao, H.-K. Qi, and Z.-Y. Sun, *Chin. Phys. C* **44**, 024001 (2020).
- [21] B. Pritychenko, E. Běták, M. Kellett, B. Singh, and J. Totans, *Nucl. Instrum. Methods Phys. Res., Sect. A* **640**, 213 (2011).
- [22] M. Wang, G. Audi, A. Wapstra, F. Kondev, M. MacCormick, X. Xu, and B. Pfeiffer, *Chin. Phys. C* **36**, 1603 (2012).
- [23] A. Ozawa, I. Tanihata, T. Kobayashi, Y. Sugahara, O. Yamakawa, K. Omata, K. Sugimoto, D. Olson, W. Christie, and H. Wieman, *Nucl. Phys. A* **608**, 63 (1996).
- [24] I. Tanihata, T. Kobayashi, O. Yamakawa, S. Shimoura, K. Ekuni, K. Sugimoto, N. Takahashi, T. Shimoda, and H. Sato, *Phys. Lett. B* **206**, 592 (1988).
- [25] K. Matsuta, K. Sato, M. Fukuda, M. Mihara, T. Yamaguchi, M. Sasaki, T. Miyake, K. Minamisono, T. Minamisono, M. Tanigaki, T. Ohtsubo, T. Onishi, Y. Nojiri, S. Momota, S. Fukuda, K. Yoshida, A. Ozawa, T. Kobayashi, I. Tanihata, J. Alonso *et al.*, *Phys. Lett. B* **459**, 81 (1999).
- [26] R. J. Charity, T. B. Webb, J. M. Elson, D. E. M. Hoff, C. D. Pruitt, L. G. Sobotka, P. Navrátil, G. Hupin, K. Kravvaris, S. Quaglioni, K. W. Brown, G. Cerizza, J. Estee, W. G. Lynch, J. Manfredi, P. Morfouace, C. Santamaria, S. Sweany, M. B. Tsang, T. Tsang *et al.*, *Phys. Rev. C* **104**, 024325 (2021).
- [27] J. W. Xia, W. L. Zhan, B. W. Wei, Y. J. Yuan, M. T. Song, W. Z. Zhang, X. D. Yang, P. Yuan, D. Q. Gao, H. W. Zhao, X. T. Yang, G. Q. Xiao, K. T. Man, J. R. Dang, X. H. Cai, Y. F. Wang, J. Y. Tang, W. M. Qiao, Y. N. Rao, Y. He *et al.*, and *Nucl. Instrum. Methods Phys. Res., Sect. A* **488**, 11 (2002).
- [28] W. L. Zhan, J. W. Xia, H. W. Zhao, G. Q. Xiao, Y. J. Yuan, H. S. Xu, K. D. Man, P. Yuan, D. Q. Gao, X. T. Yang, M. T. Song, X. H. Cai, X. D. Yang, Z. Y. Sun, W. X. Huang, Z. G. Gan, and B. W. Wei, *Nucl. Phys. A* **805**, 533c (2008).
- [29] W. L. Zhan, J. R. Dang, Q. M. Yin, B. W. Wei, J. C. Wang, X. W. Meng, Z. Y. Guo, R. R. He, Y. X. Luo, Z. Y. Sun, S. H. Jiang, W. S. Zhang, Q. J. Wang, G. H. Liu, S. X. Zhou, Y. F. Wang, G. Q. Xiao, J. X. Li, and L. J. Qing, *Sci. China Ser. A-Math.* **42**, 528 (1999).
- [30] Z. Y. Sun, W. L. Zhan, Z. Y. Guo, G. Q. Xiao, and J. X. Li, *Nucl. Instrum. Meth. Phys. Res. A* **503**, 496 (2003).
- [31] Y. Y. Yang *et al.*, *Nucl. Instrum. Methods Phys. Res., Sect. A* **701**, 1 (2013).

- [32] Y. Kanada-En'yo, Y. Kawanami, Y. Taniguchi, and M. Kimura, *Prog. Theor. Phys.* **120**, 917 (2008).
- [33] H. Iwasaki, A. Dewald, C. Fransen, A. Gelberg, M. Hackstein, J. Jolie, P. Petkov, T. Pissulla, W. Rother, and K. O. Zell, *Phys. Rev. Lett.* **102**, 202502 (2009).
- [34] L. Chamon, B. Carlson, and L. Gasques, *Comput. Phys. Commun.* **267**, 108061 (2021).
- [35] L. Chamon, *Nucl. Phys. A* **787**, 198 (2007), Proc. 9th Internat. Conf Nucl.-Nucl. Coll.
- [36] B. V. Carlson and D. Hirata, *Phys. Rev. C* **62**, 054310 (2000).
- [37] M. Cage, A. Cole, and G. Pyle, *Nucl. Phys. A* **201**, 418 (1973).
- [38] D. Y. Pang, P. Roussel-Chomaz, H. Savajols, R. L. Varner, and R. Wolski, *Phys. Rev. C* **79**, 024615 (2009).
- [39] D. Y. Pang, W. M. Dean, and A. M. Mukhamedzhanov, *Phys. Rev. C* **91**, 024611 (2015).
- [40] Y. Zhang, D. Y. Pang, and J. L. Lou, *Phys. Rev. C* **94**, 014619 (2016).
- [41] Y. P. Xu and D. Y. Pang, *Phys. Rev. C* **87**, 044605 (2013).
- [42] E. Bauge, J. P. Delaroche, and M. Girod, *Phys. Rev. C* **63**, 024607 (2001).
- [43] A. Ozawa, T. Suzuki, and I. Tanihata, *Nucl. Phys. A* **693**, 32 (2001).
- [44] B. A. Brown, *Phys. Rev. C* **58**, 220 (1998).
- [45] V. Guimarães, J. J. Kolata, E. F. Aguilera, A. Howard, A. Roberts, F. D. Becchetti, R. O. Torres-Isea, A. Riggins, M. Febrarro, V. Scarduelli, P. N. de Faria, D. S. Monteiro, J. F. P. Huiza, A. Arazi, J. Hinnefeld, A. M. Moro, E. S. Rossi, V. Morcelle, A. Barioni, and A. J. Mitchell, *Phys. Rev. C* **93**, 064607 (2016).
- [46] I. J. Thompson, *Comput. Phys. Rep.* **7**, 167 (1988).
- [47] A. Koning and J. Delaroche, *Nucl. Phys. A* **713**, 231 (2003).
- [48] A. Navin, D. W. Anthony, T. Aumann, T. Baumann, D. Bazin, Y. Blumenfeld, B. A. Brown, T. Glasmacher, P. G. Hansen, R. W. Ibbotson, P. A. Lofy, V. Maddalena, K. Miller, T. Nakamura, B. V. Pritychenko, B. M. Sherrill, E. Spears, M. Steiner, J. A. Tostevin, J. Yurkon *et al.*, *Phys. Rev. Lett.* **85**, 266 (2000).
- [49] W. Liu, J. L. Lou, Y. L. Ye, Z. H. Li, Q. T. Li, H. Hua, X. F. Yang, J. Y. Xu, H. J. Ong, D. T. Tran, N. Aoi, E. Ideguchi, D. Y. Pang, C. X. Yuan, S. M. Wang, Y. Jiang, B. Yang, Y. Liu, J. G. Li, Z. Q. Chen *et al.*, *Phys. Rev. C* **104**, 064605 (2021).